Photocatalysis
https://www.sciltp.com/journals/photocatalysis

Article

Low-Temperature Photo-Thermal Synthesis of Ammonia over K-Promoted Ru/CeO_2 Catalyst

Angel Sousa, Alejandra Rendón-Patiño, Xinhuilan Wang, Diego Mateo * and Jorge Gascon *

Advanced Catalytic Materials (ACM), KAUST Catalysis Center (KCC), King Abdullah University of Science and Technology (KAUST), Thuwal 23955-6900, Saudi Arabia
* Correspondence: diego.mateo@kaust.edu.sa (D.M.); jorge.gascon@kaust.edu.sa (J.G.)

How To Cite: Sousa, A.; Rendón-Patiño, A.; Wang, X.; et al. Low-Temperature Photo-Thermal Synthesis of Ammonia over K-Promoted Ru/CeO_2 Catalyst. *Photocatalysis* **2025**, *1*(1), 2. https://doi.org/10.53941/photocatalysis.2025.100002

Received: 12 July 2025
Revised: 28 September 2025
Accepted: 14 October 2025
Published: 16 October 2025

Abstract: Haber-Bosch process has enabled large-scale ammonia (NH_3) production for over a century. Yet, its high energy demand and carbon footprint reinforces the need to develop new approaches for sustainable NH_3 synthesis. In this study, a K-promoted Ru/CeO_2 catalyst is investigated for photo-thermal NH_3 synthesis under continuous flow conditions, leveraging light and heat to enhance catalytic efficiency. The optimized Ru(3)/CeO_2 catalyst achieved an NH_3 production rate of 20 mmol g^{-1} h^{-1} at 350 °C and 20 bar, representing the highest reported performance for a photo-thermal system. Mechanistic studies revealed that light-driven charge transfer processes accelerate NH_3 formation via an associative pathway, as confirmed by in-situ DRIFTS analysis. Notably, the system remained stable for over 50 h without deactivation. Beyond NH_3 synthesis, the catalyst also demonstrated high efficiency for photo-thermal NH_3 decomposition, achieving 656 mmol H_2 g^{-1} h^{-1} at a temperature as low as 215 °C, a significant improvement over conventional thermocatalytic methods. These findings highlight the potential of Ru/CeO_2-based catalysts for integrated photo-thermal NH_3 synthesis and decomposition, offering a promising route for sustainable NH_3-based energy storage and utilization.

Keywords: photo-thermal catalysis; ammonia synthesis; ruthenium; ceria

1. Introduction

The Haber-Bosch (HB) process has enabled large-scale ammonia (NH_3) production for fertilizers, chemicals, and numerous industrial applications. Currently, 240 million metric tons of NH_3 are produced per year, with over 96% being manufactured via HB method [1,2]. However, despite its significant contribution to agriculture and human development, NH_3 synthesis accounts for nearly 2% of the world's energy consumption [3]. In light of this, focus has shifted towards strategies that could allow for the direct utilization of renewable energy for the synthesis of NH_3, with a particular emphasis on harnessing sunlight [4–6].

Since the seminal works of Fujishima and Honda in the 1970's, photocatalysis introduced not only a novel pathway for chemical production, but also a shift in perspective towards a future decoupled from fossil fuel consumption. The use of sunlight to drive chemical reactions presents a promising approach for sustainable development while reducing environmental impact [7,8]. However, low conversion levels and slow reaction kinetics prevent its scalability for industrial applications. Moreover, traditional photocatalytic systems are restricted to UV light, leaving 97% of the solar spectrum unused [9,10]. To overcome this challenge, photo-thermal catalysis has emerged as an innovative approach to produce chemicals by leveraging the synergistic effect of photo- and thermochemical processes of sunlight [11–14]. In this synergy, UV-visible photons generate electron-hole pairs, while visible and IR light promote localized heating on the surface of the catalyst. Consequently, thermodynamic barriers are lowered, enabling reactions pathways with diminished energy requirements [15–17].

As a result, photo-thermally driven reactions have attracted considerable attention, and their application in highly energy-intensive processes like NH_3 production holds significant promise.

In this context, iron (Fe)-based catalysts have been traditionally employed for NH_3 synthesis. However, limitations such as high operating temperatures and pressures have driven research towards catalytic systems able to operate under milder conditions [18,19]. In view of this, ruthenium (Ru)-based catalysts have gained significant attention for their enhanced catalytic activity, particularly at moderate reaction conditions [20–23]. Nevertheless, only a few studies have investigated supported Ru NPs for photo-thermal NH_3 synthesis. Recently, a TiO_2-supported Ru catalyst was reported, achieving nearly 240 μmol g^{-1} h^{-1} at 350 °C and 10 bar [24]. On another note, Peng and co-workers reported two Cs-promoted Ru catalysts supported on strontium titanate and ZrO_2, which achieved 3.6 and 5.1 mmol g^{-1} h^{-1}, respectively, at 350 °C and ambient pressure. In these works, authors emphasized the importance of the photo-thermal strategy, while also pointing out the critical role of promoters in enhancing NH_3 production.

In fact, the incorporation of promoters such as alkali and alkaline earth metals is known to dramatically increase catalytic activity via structural or electronic promotion [25]. Potassium (K), for instance, donates electrons to increase the electron density at metal active sites, thereby facilitating N_2 bond activation, stabilizing intermediates and modulating adsorption properties of products [26,27]. In addition, alkali promoters can alleviate excessive hydrogen coverage of the metal surface by facilitating N_2 hydrogenation, therefore limiting the effect of hydrogen poisoning. However, promotion alone is not sufficient to prevent this effect, and catalysts may face deactivation beyond a certain point. To tackle this issue, metal oxide supports such as TiO_2, CeO_2, and V_2O_5, are frequently utilized due to their ability to enhance hydrogen spillover and, consequently, prevent H poisoning [28–31].

In particular, the presence of oxygen vacancies within CeO_2 has been shown to promote N≡N activation in the NH_3 synthesis reaction by increasing electron density at the Ru sites [28]. Ru's affinity for H_2 facilitates the reduction of CeO_2, further increasing the number of oxygen vacancies, which, in its turn, leads to enhanced catalytic performance. In addition, the strong metal-support interaction (SMSI) between Ru and CeO_2 tends to stabilize Ru nanoparticles (NPs), resulting in a fine and homogeneous dispersion throughout the catalyst while preventing their sintering [32–35]. In fact, SMSI can be evidenced by the formation of a suboxide around metallic particles, effectively resulting in partial or total encapsulation of the metal by the support. Beyond structural effects, SMSI also facilitates electronic metal-support interaction (EMSI), inducing electronic perturbations and charge transfer between metal and support. Such interactions may alter the adsorption and dissociation properties of reactant molecules, consequently enhancing catalytic performance [36]. Nevertheless, and despite all these promising features, the use of CeO_2 has been surprisingly overlooked in the photo-thermal catalytic production of NH_3.

Herein, we report a K-promoted Ru-based catalyst supported on CeO_2 for the photo-thermal ammonia synthesis under continuous flow configuration. Under optimal conditions, the photo-thermal catalyst exhibited an NH_3 production rate of approximately 20 mmol g^{-1} h^{-1} and a solar-to-ammonia (STA) conversion efficiency of 0.17%. To the best of our knowledge, these values represent one of the highest production rates and STA conversion efficiencies reported to date for the photo-thermal ammonia synthesis. Mechanistic studies have evidenced the crucial role of light in accelerating the ammonia production through the interplay between photo- and thermal contributions of light. Furthermore, in situ DRIFTS analysis highlighted the critical role of light in accelerating the chemical reaction, offering mechanistic insights supporting an associative reaction pathway in both the absence and presence of light. Last but not least, the catalyst has shown a remarkable activity for the photo-thermal NH_3 cracking reaction in the absence of external heating, thus closing the loop for a sustainable and energy-efficient ammonia synthesis/decomposition cycle.

2. Results

K-promoted Ru(x)/CeO_2 catalysts (where x stands for the Ru wt.% content, from 1 to 4 wt.%) were obtained via wet impregnation of commercially available CeO_2 with different amounts of Ru and K precursors followed by calcination and reduction treatments, as described in Supporting Information and illustrated in Figure 1.

First, H_2 Temperature Programmed Reduction (H_2-TPR) was measured for pristine CeO_2 and K-promoted Ru(2)/CeO_2 samples (Figure S1). Previous studies have demonstrated that the H_2-TPR profile of CeO_2 exhibits two main features: (1) reduction of surface oxygen species leading to vacancy formation, and (2) reduction of bulk CeO_2 due to outwards O diffusion, an undesirable phenomenon that triggers loss of particle shape, negatively impacting the catalytic performance [37]. The first reduction typically happens at temperatures below 500 °C while the second requires temperatures above 600 °C [38,39]. Figure S1 shows a peak located at 500 °C for pristine CeO_2 attributed to the reduction of surface oxygen species. On the other hand, the reduction profile of K-promoted

Ru(2)/CeO_2 catalyst exhibits two regions of interest: a peak at 130 °C for the reduction of RuO_2, and a broader peak at higher temperature (250 °C) attributed to the first reduction of the CeO_2 support. These results indicated that the presence of Ru increased the reducibility of CeO_2. Therefore, based on H_2-TPR analysis, all catalysts were pre-reduced at 350 °C under a 6 vol% H_2/Ar flow for 2 h and subsequently passivated under 5 vol% O_2/N_2 at room temperature for 1 h.

Subsequently, pristine CeO_2, K-promoted CeO_2 and K-promoted Ru(x)/CeO_2 samples with different Ru contents were characterized via Powder X-ray Diffraction (PXRD) analysis (Figures S2 and S3a). The peaks at 28.6°, 33.1°, 47.6° and 56.4° were assigned to the diffraction planes (111), (200), (220) and (311) of CeO_2 fluorite (Fm3m). The small peaks observed at 40.5° and 44.1° were attributed to the reflection planes (111) of potassium chloride (KCl) and (101) of metallic Ru, respectively. The successful incorporation of Ru in the CeO_2 support was corroborated by Inductively Coupled Plasma Optical Emission Spectrometry (ICP-OES) (Table S1). High-Resolution Transmission Electron Microscopy (HR-TEM) images of the K-promoted Ru(3)/CeO_2 confirmed the homogeneous distribution of Ru NPs throughout the CeO_2 support with a particle size distribution of 1.1 ± 0.3 nm (Figure 1) [40]. Based on these images, it was possible to measure a lattice distance of 0.205 and 0.311 nm attributable to the (101) plane of metallic Ru and (111) plane of CeO_2, respectively, in good agreement with the main peaks observed in XRD (Figures 1 and S4). Moreover, additional HAADF-STEM analysis coupled with elemental mapping not only demonstrated the presence of Ru and K decorating the surface of the CeO_2 support, but also the strong metal-support interaction between Ru and CeO_2, as evidenced by the encapsulation of metallic nanoparticles by the metal oxide (Figures S5 and S6).

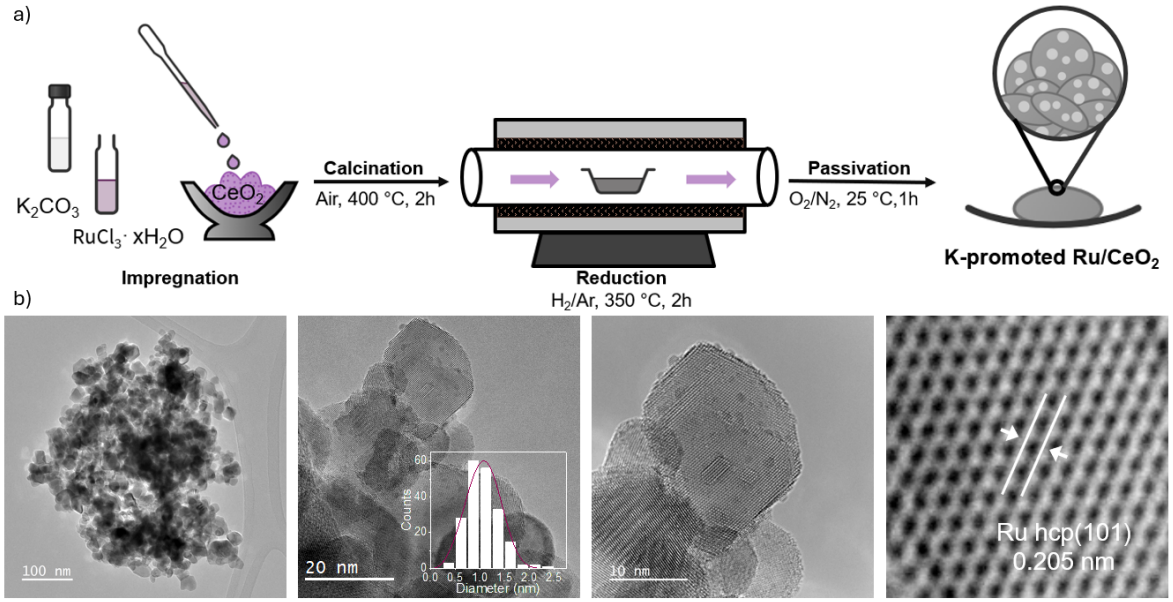

Figure 1. (**a**) Procedure for catalyst synthesis. (i) Preparation of a solution of ruthenium (III) chloride and potassium carbonate in Milli-Q® water. (ii) Impregnation of cerium oxide with the resulting solution from (i). (iii) Calcination at 400 °C for 2 h. (iv) Reduction at 350 °C for 2 h in a gas mixture consisting of 6 vol% H_2 in Argon (Ar). (v) Passivation with diluted O_2 (5 vol% in N_2) at room temperature for 1 h. (**b**) HR-TEM images of the K-promoted Ru(3)/CeO_2 sample. Bottom right image shows the interplanar distance corresponding to the (101) plane of metallic Ru. Inset shows the particle size distribution.

The degree of defects in the CeO_2 lattice upon Ru incorporation was evaluated using Raman spectroscopy under nitrogen (N_2) atmosphere. As shown in Figure S7, one main peak is observed in the CeO_2 spectrum at 462 cm^{-1} and a shouldering at 600 cm^{-1}, which correspond to the F_{2g} and defect-induced (D) vibrational modes of fluorite [41]. These vibrational modes represent the symmetrical stretching of oxygen atoms around cerium ions in the fluorite structure, consistent with the PXRD findings. Upon Ru incorporation, no additional peaks were observed, however, a red-shift and a broadening of the F_{2g} peak were clearly discernible. These alterations in the spectra are in line with previous findings and indicate the introduction of defects within the CeO_2 lattice as Ru is incorporated [35,41]. To compare the extent of this effect across samples with varying Ru content, we calculated the ratio between the D and F_{2g} peak intensities I_{600}/I_{462}, which is correlated with the amount of intrinsic defects, such as oxygen vacancies, within the CeO_2 lattice. According to the values in Table S2, while oxygen vacancies are present in pristine CeO_2, they constitute merely 0.01 ratio of the lattice bonds. However, as the Ru content

increases across the samples, the concentration of these defects gradually rises, reaching a maximum ratio of 0.32. The K-promoted CeO_2 sample did not exhibit significant differences compared to pristine CeO_2 (Figure S3b).

Complementarily, to identify the surface chemical species present in our catalyst and further analyze the introduction of defects on the CeO_2 structure upon Ru loading, X-ray photoelectron spectroscopy (XPS) analysis was conducted on pristine CeO_2 and K-promoted Ru(3)/CeO_2 sample as representative of the Ru(x)/CeO_2 samples (Figure S8). The O 1s core level spectra were fitted into two peaks centered at 529.0 and 530.7 eV, corresponding to lattice oxygen (O_L) and O^{2-} in oxygen deficient regions (O_V), respectively [42]. The ratio O_V/O_L calculated for the samples were 0.1 and 0.5 for the CeO_2 and K-promoted Ru(3)/CeO_2 samples, denoting an increase in surface oxygen vacancies upon Ru incorporation, in accordance with the Raman analysis. For the Ce 3d spectra of pristine CeO_2, ten peaks were fitted corresponding to the pairs of spin-orbit doublets, with five peaks at 882.0, 888.4, 897.9, 907.1 and 916.4 eV for Ce^{4+}, and other five peaks located at 880.3, 884.1, 895.9 and 900.5 and 902.1 eV for Ce^{3+} [43,44]. In this case, the calculated Ce^{3+}/Ce^{4+} ratio, which represents the concentration of oxygen vacancies in the material, was 0.40. Upon incorporation of Ru, the Ce^{3+}/Ce^{4+} ratio increased up to 0.53, indicating the generation of defects on the CeO_2 lattice. Indeed, XPS data aligns with the Raman results, indicating that Ru incorporation promotes the formation of oxygen vacancies. The Ru 3p spectrum could be fitted into two main contributions at 462.3 and 484.5 eV, corresponding to metallic Ru, together with two smaller contributions at 464.8 and 486.9 eV for RuO_x attributable to the passivation layer generated during the synthesis of the catalyst (see Supplementary Information) [45]. Interestingly, these peaks displayed a significant shift towards higher binding energies (~0.9 eV), thus indicating the generation of positively charged $Ru^{\delta+}$ species as a result of the strong interaction between CeO_2 and Ru [46].

Figure S9 shows the EPR spectra of CeO_2, K-promoted CeO_2 and K-Ru/CeO_2 measured at room temperature after their calcination and reduction. Here, EPR was used as a diagnostic tool for the formation of Ce^{+4}–O^{-}–Ce^{3+} species, and, therefore, for oxygen vacancy detection. CeO_2 displays several well-defined resonances in the g = 1.8–2.2 region, characteristic of localized Ce^{3+} species and trapped electrons associated with oxygen vacancy sites [47,48]. Upon K addition, the features become slightly attenuated, consistent with the expected effect of K in modifying the electron density of CeO_2. In contrast, the incorporation of Ru led to a marked transformation of the spectrum, with the broadening and increase in intensity of the resonance centered at $g \approx 1.96$, which corresponds to the Ce^{+4}–O^{-}–Ce^{3+} species. This signal evolution reflects a substantial increase in Ce^{3+} concentration as Ru strongly promotes reducibility of the support, indicating the formation of oxygen vacancies upon Ru addition. Indeed, these findings are in good agreement with the trends observed by XPS, Raman and H_2-TPR.

UV-vis-NIR absorption measurements were performed for all samples to assess their light absorption properties. All spectra exhibited a strong absorption peak around 320–330 nm, corresponding to the characteristic interband transitions of CeO_2 (Figure S10) [49]. Remarkably, light absorption in the visible and IR regions increased with higher Ru content, and RuO_x plasmonic bands were distinctly apparent in the samples with the highest Ru loading (inset of Figure S10) [36]. These results indicate that the introduction of Ru dramatically improved the absorption properties of the Ru/CeO_2 catalysts.

The catalytic performance of K-promoted Ru(x)/CeO_2 samples for photo-thermal ammonia synthesis was investigated under continuous flow configuration at 350 °C and 10 bar, using a 300 W Xe lamp with a light intensity of 3.3 W cm^{-2}. First, we studied the effect of the Ru loading on the catalytic performance. As shown in Figure 2a, the NH_3 production increased with Ru content up to 3 wt.%, achieving a maximum production rate of 13 mmol g^{-1} h^{-1}. A higher Ru content led to a decrease in the catalytic performance, probably due to a larger particle size of 1.5 ± 0.7 nm as evidenced by HRTEM analysis (Figure S11). When it comes to the K promoter, 5.0 wt.% concentration displayed the best catalytic results, likely due to a compromise between the positive effect of the alkali and an excessive coverage of the Ru active sites (Figure 2b). In view of these findings, subsequent studies were performed with the 5.0 wt.% K-promoted Ru(3)/CeO_2 sample unless otherwise indicated. As per Figure 2c, we observed a positive relationship between the catalytic activity and the operating pressure up to 20 bar, reaching a remarkable NH_3 production rate of nearly 20 mmol g^{-1} h^{-1}. To the best of our knowledge, this productivity represents the highest value reported for the photo-thermal ammonia synthesis under continuous flow configuration (Table S3).

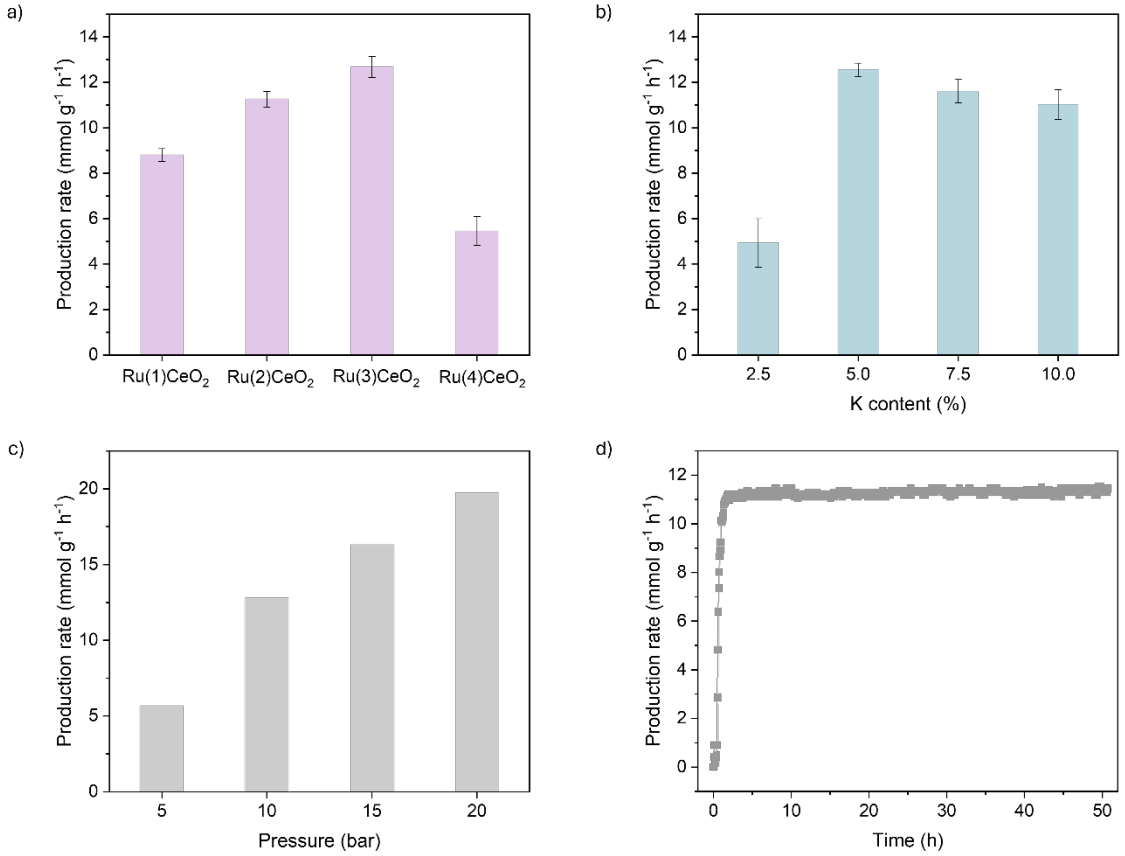

Figure 2. Study of the influence of (**a**) Ru content, (**b**) K content and (**c**) operating pressure on the catalytic activity of K-promoted Ru(x)/CeO_2 catalysts for the photo-thermal NH_3 synthesis. (**d**) Long-term stability test over K-promoted Ru(3)/CeO_2. Reaction conditions: H_2/N_2 = 3, GHSV = 20,000 mL g^{-1} h^{-1}, 350 °C, 10 bar, light intensity 3.3 W cm^{-2}.

After optimizing the Ru and K content, our focus shifted to evaluating the stability of the catalyst under reaction conditions. As can be seen from Figure 2d, the catalyst maintained its performance over 50 h without any sign of deactivation, highlighting the remarkable stability of the K-promoted Ru(3)/CeO_2 catalyst. Additional HRTEM images of the spent sample revealed the absence of particle sintering or agglomeration (Figure S12). Complementarily, no phase changes were observed in the PXRD patterns compared to the fresh sample, thus confirming the excellent stability of the catalyst under operation (Figure S13).

Next, we conducted an in-depth assessment of the mechanisms underlying the photo-thermal NH_3 synthesis on K-promoted Ru(3)/CeO_2 catalyst. Initially, to distinguish between photo-induced and thermal effects, experiments were performed under direct and indirect illumination at varying light intensities. For the indirect illumination tests, a thin layer (<1 mm) of Ti_2O_3 was placed on top of the catalytic bed to capture light and convert into heat. This strategy ensured the suppression of photo-effects while replicating the temperature profile of the catalytic bed under direct light illumination, mimicking a purely thermocatalytic pathway [50]. Under indirect illumination, NH_3 production rate expressed a clear exponential behavior with respect to light intensity, characteristic of a thermocatalytic pathway dominated by pure thermal effects (Figure 3a). On the other hand, under direct illumination, the production rate increased significantly, exhibiting a linear dependance with light intensity for values below 2.5 W cm^{-2}, characteristic of a photocatalytic pathway (Figure 3a). As observed in Figure S14, both sets of experiments reached similar temperatures under reaction conditions, thus indicating that this methodology provides comparable photo-thermal heating while suppressing any photochemical contribution. The difference in NH_3 production rate between both direct and indirect illumination increased upon augmenting the power density up to 2.2 W cm^{-2}, suggesting that non-thermal effects are dominant at those irradiances. Nevertheless, when the light intensity increased beyond 2.5 W cm^{-2}, an inflection point was observed, and the production rate decreased for the experiment directly illuminated. According to the literature, there are two possible scenarios that explain this finding: (1) the increment in light intensity, and therefore in temperature, increases the kinetic energy in the system, enhancing the recombination rate of charge carriers, which in its turn

mitigates the photochemical contribution and results in lower performances; (2) the increment in temperature, instead of contributing for the NH_3 formation, shifts the equilibrium towards the endothermic back reaction, thus decomposing any produced NH_3 [51,52]. Therefore, although a contribution from the reverse reaction cannot be fully discarded, we attribute the performance drop observed at high light intensities to charge carrier recombination events at elevated temperatures, as the small amount of NH_3 produced during our experiments suggests that its formation followed by decomposition is unlikely to happen, especially under high H_2 partial pressure in the reaction mixture [53,54]. The crucial role of light becomes even more evident when calculating the values of apparent activation energy for both experiments under dark and light conditions, resulting in 254 kJ mol^{-1} and 134 kJ mol^{-1}, respectively. These findings highlight the critical role of light in lowering energy barriers and enabling more efficient catalytic pathways.

In view of the light intensity-dependent experimental results, we also calculated the solar-to-ammonia (STA) conversion efficiency of our system under optimal conditions to assess its potential applicability:

$$\text{STA}\ (\%) = \frac{\Delta G_{NH_3}\left(\text{J mol}^{-1}\right) \times \text{NH}_3\ \text{formed (mol)}}{\text{total incident power (W)} \times \text{reaction time (s)}} \times 100$$

where ΔG_{NH3} is the Gibbs free energy required for NH_3 formation at 350 °C (ΔG_{NH3} = 15.7 kJ mol^{-1}); the total incident power is calculated from the overall irradiance (W m^{-2}) and the irradiation area (m^2) [55]. It is worth reminding that, to include the energy costs associated with the temperature and pressure requirements in our efficiency calculations, we subtracted the NH_3 production under thermal conditions to the total NH_3 production under photo-thermal regime.

Therefore, based on the above equation and assumptions, we obtained a STA of 0.17% at 10 bar and 350 °C under 2.2 W cm^{-2} power density, a value that is comparable with the highest reported efficiencies for a photo-thermal ammonia synthesis system [56,57]. Considering previous estimates indicating that STA conversion efficiencies above 0.1% are necessary to compete with the conventional Haber-Bosch route for ammonia production as a nitrogen fertilizer, the photo-thermal system presented here emerges as a promising candidate for solar-driven fertilizer synthesis [58].

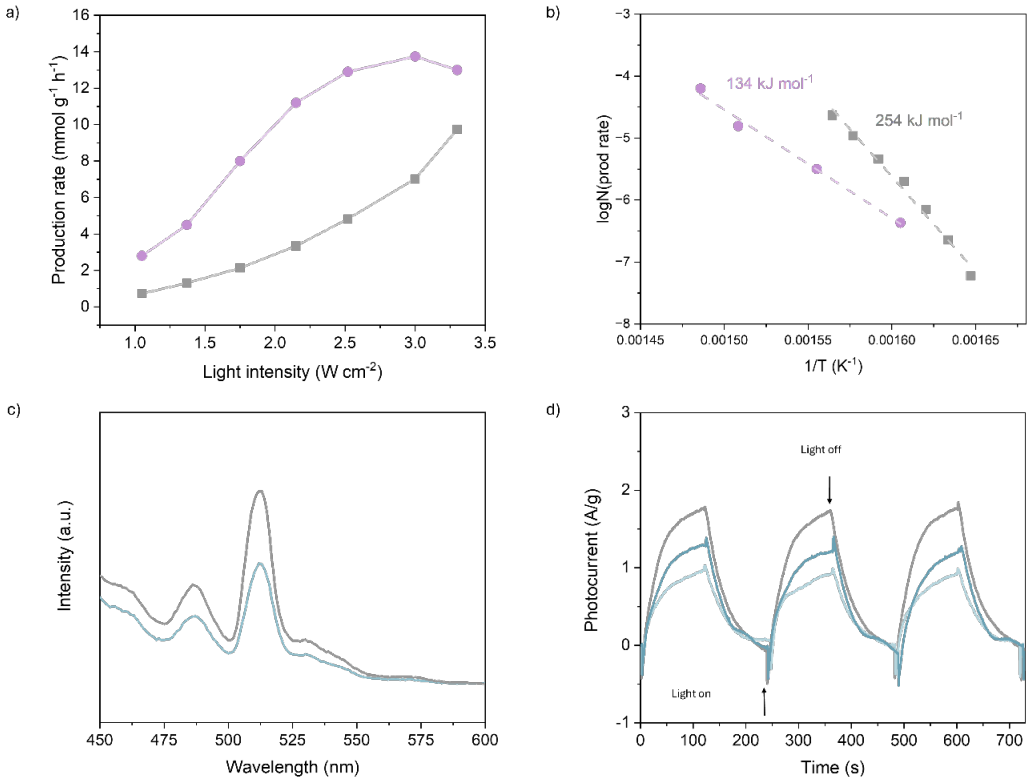

Figure 3. (**a**) Light intensity experiments under direct (pink) and indirect (gray) illumination at different light intensities. Reaction conditions: H_2/N_2 = 3, GHSV = 20,000 mL g^{-1} h^{-1}, 350 °C, 10 bar. (**b**) Activation energies for the experiments under light (pink) and dark (gray) conditions. (**c**) Steady-state photoluminescence (PL) measurements of pristine CeO_2 (gray) and K-promoted Ru(3)/CeO_2 (blue) samples. (**d**) Transient photocurrent of K-promoted Ru(3)/CeO_2 sample under 400 (gray), 300 (blue) and 200 mW cm^{-2} (light gray) light intensity.

Complementarily, steady-state photoluminescence (PL) and transient photocurrent measurements confirmed the presence of photochemical effects in our system. As shown in Figure 3c, pristine CeO_2 displayed two prominent emission peaks at 487 and 512 nm, attributable to defect states, including oxygen vacancies with trapped electrons [59]. Curiously, the K-promoted Ru(3)/CeO_2 sample exhibited a lower photoluminescence compared to pristine CeO_2. This decrease in the PL intensity indicates an effective charge transfer from the CeO_2 to the Ru sites, improving the overall charge separation efficiency. In fact, the XPS analysis of the spent sample revealed additional evidence for this electron transfer from ceria towards Ru. As can be seen in Figure S15, the Ru 3p peaks exhibited a shift of approximately 0.7 eV towards lower binding energies compared to the fresh sample. Altogether, these results suggest a transfer of photo-excited electrons from ceria, most likely from Ce^{3+} and oxygen vacancies, and the generation of electron-rich Ru sites. These electron-rich Ru species can activate H_2 by dissociative adsorption, thus creating Ru-H hydrides and increasing its reactivity for NH_3 synthesis, as we will elaborate below through in situ DRIFTS experiments. In addition, transient photocurrent of K-promoted Ru(3)/CeO_2 demonstrated the presence of photoactivity upon illumination, exhibiting a positive correlation with light intensity (Figure 3d).

To deepen our understanding of the reaction mechanism, in-situ DRIFTS was performed to monitor the formation of intermediates during the reaction in the presence and absence of light for the K-promoted Ru(3)/CeO_2 catalyst. In absence of light, three bands located at 1980, 1600 and 1355 cm^{-1} became prominent with the temperature rise (Figure 4b, blue dashed lines). These bands are typically associated with the formation of Ru–H species, indicating the onset of the H_2 dissociation process at nearly 100 °C [60–62]. Indeed, this finding correlates well with our H_2-TPR results, which showed H_2 consumption at a similar temperature (Figure S1). In addition, absorption bands ascribed to NH_x intermediates appear at temperatures above 200 °C mainly in the range of 1340–1550 cm^{-1} and at 1240 cm^{-1} (grey highlights). Interestingly, a broad feature corresponding to the N–N stretching vibration of N–NH_x adsorbed molecules was observed in the range of 1080–1170 cm^{-1} (pink highlight) [63–65]. Although faint, this feature is crucial for confirming the existence of an associative pathway for ammonia production in the absence of light. Additionally, a peak shift from 1865 to 1760 cm^{-1} related to Ru–H and N–H interactions was observed, possibly indicating a change in surface coverage of the active sites as the reaction evolved [66]. On a second scenario, upon light exposure, subtle yet significant spectral changes emerged (Figure 4c). First, the main features related to NH_x (grey highlights) and N–NH_x (pink highlights) appear sharper and enhanced at temperatures as low as 120 °C, evidencing that the introduction of light accelerates the NH_3 reaction at lower temperatures. Second, Ru–H bands were no longer detected, evidencing a fast transition between Ru–H and NH_x production upon irradiation. These observations indicate that negatively charged Ru sites induce a fast hydrogenation of adsorbed N_2 on the catalyst surface, thus boosting the generation of NH_3. It is worth reminding that traditional Ru-based catalysts are prone to suffer from hydrogen poisoning. In our case, we hypothesize that the light-induced rapid hydrogenation of adsorbed nitrogen circumvents the deactivation of the catalyst due to hydrogen blockage, as confirmed by the pressure-dependent experiments exhibiting a positive relationship between H_2 partial pressure and catalytic activity (Figure 2c). In fact, increasing the operating pressure from 10 to 20 bar under dark conditions had an obvious negative effect on the catalytic performance, thus confirming that, in the absence of illumination, hydrogen can block Ru active sites and therefore inhibit the ammonia synthesis reaction (Figure S16). Altogether, these findings demonstrate that, despite following a similar associative mechanism, the NH_3 synthesis is dramatically accelerated under light exposure.

Besides its well-known application as a fertilizer, ammonia has recently gained considerable attraction as a potential hydrogen carrier by virtue of its high volumetric and gravimetric energy density. Nonetheless, in contrast to the synthetic route, the NH_3 decomposition process is far from being optimized and harsh temperatures in the order of 500–600 °C are commonly required to achieve significant conversion rates. Recently, some works evidenced the versatility and efficiency of photo-thermal catalysis for NH_3 cracking [67,68]. In this context, and given the promising features of our catalyst for the photo-thermal NH_3 synthesis, we investigated its application for the light-induced NH_3 cracking reaction in the absence of external heating. As observed in Figure S17, a remarkable NH_3 conversion of 27% was achieved, corresponding to 656 mmol g_{cat}^{-1} h^{-1} of H_2 production at temperatures as low as 215 °C. In contrast, performing the experiment in absence of light at the same temperature led to no observable conversion. In fact, conventional thermocatalytic Ru-based catalysts require from considerably harsher reaction conditions to achieve comparable catalytic performances. Moreover, to the best of our knowledge, this is the highest reported value for photo-thermal NH_3 cracking to date, as observed in Table S4. To have a better insight into the exceptional catalytic activity of the K-promoted Ru(3)/CeO_2 catalyst in the NH_3 decomposition reaction, we performed NH_3-TPD measurements under light and dark conditions. As per Figure S18, the main desorption peak of H_2 under radiation starts at 185 °C, reaching its maximum at 250 °C, together with a small desorption at low temperature attributable to weakly physisorbed NH_3. In stark contrast, the desorption of H_2 under dark conditions starts only at temperatures above 246 °C, roughly 60 °C higher temperature compared

to the experiment under illumination. Therefore, NH_3-TPD experiments suggest that light could enhance the NH_3 decomposition reaction by facilitating the H_2 desorption from the catalyst surface. In this case, the generation of electron-rich Ru species under illumination facilitates the H_2 recombinative desorption at lower temperatures. Overall, these results demonstrate the potential of our K-promoted Ru(3)/CeO_2 catalyst to efficiently perform both the synthesis and decomposition of NH_3 under photo-thermal conditions, closing the loop for a more sustainable production and utilization of ammonia in future low-carbon economies.

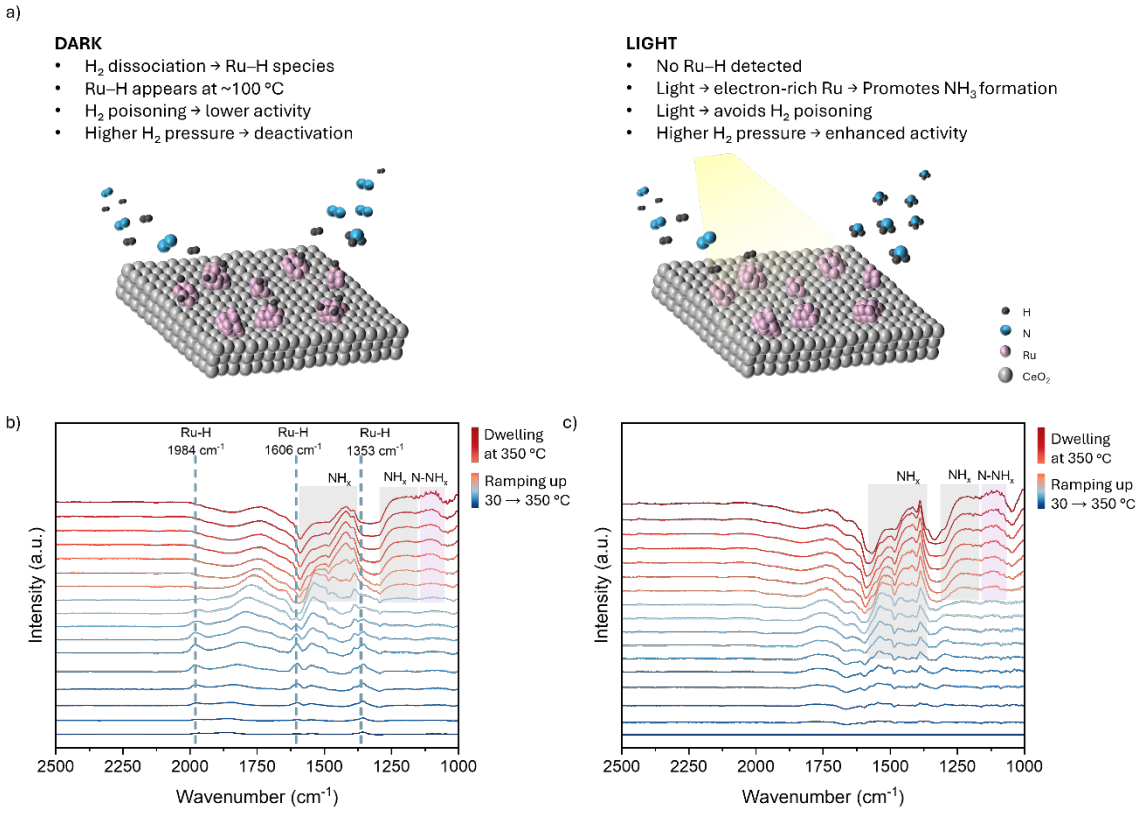

Figure 4. (**a**) Schematic illustration summarizing the effect of light illumination on the catalytic surface. In-situ DRIFTS analysis of K-promoted Ru(3)/CeO_2 under H_2/N_2 (3:1) at 10 bar with increased temperature upon (**b**) dark and (**c**) light conditions.

3. Conclusions

In summary, this study introduces a bifunctional K-promoted Ru(3)/CeO_2 catalyst for the photo-thermal NH_3 synthesis and decomposition reactions under continuous flow configuration. After systematic optimization, a NH_3 production rate of nearly 20 mmol g^{-1} h^{-1} was achieved at 350 °C and 20 bar under light irradiation. Mechanistic investigations under direct and indirect illumination confirmed the predominance of a non-thermal pathway in combination with thermal contribution. Steady-state photoluminescence and transient photocurrent measurements provided evidence of significant photo-induced effects within our system. Furthermore, in situ DRIFTS analysis highlighted the critical role of light in accelerating the chemical reaction, offering mechanistic insights supporting an associative reaction pathway in both the absence and presence of light.

Supplementary Materials

The additional data and information can be downloaded at: https://media.sciltp.com/articles/others/25101516 58331321/Photocatalysis-2508000100-SI-done.pdf. Experimental details (materials and reagents and catalyst preparation), PXRD, H_2-TPR, EPR, ICP-OES, Raman spectroscopy, PL, Transient photocurrent measurements, in situ DRIFTS, HR-TEM, STEM-HAADF, XPS, UV-vis diffuse reflectance spectroscopy, NH_3-TPD and Photo-thermal NH_3 synthesis. References [69–79] are cited in the supplementary materials.

Author Contributions

A.S.: methodology, investigation, writing—original draft preparation; A.R.-P.: methodology, investigation; X.W.: methodology, investigation, D.M.: conceptualization, data curation, supervision, writing—original draft preparation; J.G.: conceptualization, supervision, writing—reviewing and editing. All authors have read and agreed to the published version of the manuscript.

Funding

Funding for this work was provided by King Abdullah University of Science and Technology (KAUST).

Data Availability Statement

Data will be made available upon request.

Acknowledgments

The authors give special thanks to Eganathan Kaliyamoorthy and Abdel Hamid Emwas for their assistance with the ICP-OES and EPR measurements, respectively.

Conflicts of Interest

The authors declare no conflict of interest.

Use of AI and AI-Assisted Technologies

This manuscript was prepared with the assistance of ChatGPT to improve linguistic readability. After using this tool, the authors carefully reviewed and edited the content as needed and take full responsibility for the content of the published article.

References

1. Statista Research Department Production Capacity of Ammonia Worldwide from 2018 to 2021, with a Forecast for 2026 and 2030. *Online* **2023**, *2030*, 2030.
2. Ye, D.; Tsang, S.C.E. Prospects and Challenges of Green Ammonia Synthesis. *Nat. Synth.* **2023**, *2*, 612–623. https://doi.org/10.1038/s44160-023-00321-7.
3. Kyriakou, V.; Garagounis, I.; Vourros, A.; et al. An Electrochemical Haber-Bosch Process. *Joule* **2020**, *4*, 142–158. https://doi.org/10.1016/j.joule.2019.10.006.
4. Mateo, D.; Cerrillo, J.L.; Durini, S.; et al. Fundamentals and Applications of Photo-Thermal Catalysis. *Chem. Soc. Rev.* **2021**, *50*, 2173–2210. https://doi.org/10.1039/d0cs00357c.
5. Huang, P.W.; Hatzell, M.C. Prospects and Good Experimental Practices for Photocatalytic Ammonia Synthesis. *Nat. Commun.* **2022**, *13*, 7908. https://doi.org/10.1038/s41467-022-35489-7.
6. Garvey, S.M.; Davidson, E.A.; Wagner-riddle, C.; et al. Emerging Opportunities and Research Questions for Green Ammonia Adoption in Agriculture and Beyond. *Nat. Rev. Clean Technol.* **2025**, *1*, 10–11. https://doi.org/10.1038/s44359-024-00012-2.
7. Usubharatana, P.; McMartin, D.; Veawab, A.; et al. Photocatalytic Process for CO_2 Emission Reduction from Industrial Flue Gas Streams. *Ind. Eng. Chem. Res.* **2006**, *45*, 2558–2568. https://doi.org/10.1021/ie0505763.
8. Sun, X.; Jiang, S.; Huang, H.; et al. Solar Energy Catalysis. *Angew. Chem.* **2022**, *134*, e202204880. https://doi.org/10.1002/ange.202204880.
9. Beil, S.B.; Bonnet, S.; Casadevall, C.; et al. Challenges and Future Perspectives in Photocatalysis: Conclusions from an Interdisciplinary Workshop. *JACS Au* **2024**, *4*, 2746–2766. https://doi.org/10.1021/jacsau.4c00527.
10. Qu, Y.; Duan, X. Progress, Challenge and Perspective of Heterogeneous Photocatalysts. *Chem. Soc. Rev.* **2013**, *42*, 2568–2580. https://doi.org/10.1039/c2cs35355e.
11. Luo, S.; Ren, X.; Lin, H.; et al. Plasmonic Photothermal Catalysis for Solar-to-Fuel Conversion: Current Status and Prospects. *Chem. Sci.* **2021**, *12*, 5701–5719. https://doi.org/10.1039/d1sc00064k.
12. Zhang, J.; Chen, H.; Duan, X.; et al. Photothermal Catalysis: From Fundamentals to Practical Applications. *Mater. Today* **2023**, *68*, 234–253. https://doi.org/10.1016/j.mattod.2023.06.017.
13. Song, C.; Wang, Z.; Yin, Z.; et al. Principles and Applications of Photothermal Catalysis. *Chem Catal.* **2022**, *2*, 52–83. https://doi.org/10.1016/j.checat.2021.10.005.
14. Mateo, D.; Sousa, A.; Zakharzhevskii, M.; et al. Challenges and Opportunities for the Photo-(Thermal) Synthesis of Ammonia. *Green Chem.* **2023**, *26*, 1041–1061. https://doi.org/10.1039/d3gc02996d.

15. Zhang, Z.; Hu, X. Visible-Light-Driven Catalytic Deracemization of Secondary Alcohols. *Angew. Chem.* **2021**, *133*, 23015–23020. https://doi.org/10.1002/ange.202107570.
16. Ziegenbalg, D.; Pannwitz, A.; Rau, S.; et al. Comparative Evaluation of Light-Driven Catalysis: A Framework for Standardized Reporting of Data**. *Angew. Chem. Int. Ed.* **2022**, *61*, e202114106. https://doi.org/10.1002/anie.202114106.
17. Khan, I.S.; Garzon-Tovar, L.; Mateo, D.; et al. Metal-Organic-Frameworks and Their Derived Materials in Photo-Thermal Catalysis. *Eur. J. Inorg. Chem.* **2022**, *2022*, e202200316. https://doi.org/10.1002/ejic.202200316.
18. Schlögl, R. Catalytic Synthesis of Ammonia-A "Never-Ending Story"? *Angew. Chem. Int. Ed.* **2003**, *42*, 2004–2008. https://doi.org/10.1002/anie.200301553.
19. Liu, H. Ammonia Synthesis Catalyst 100 Years: Practice, Enlightenment and Challenge. *Cuihua Xuebao/Chin. J. Catal.* **2014**, *35*, 1619–1640. https://doi.org/10.1016/S1872-2067(14)60118-2.
20. Ozaki, A. Development of Alkali-Promoted Ruthenium Catalyst for Ammonia Synthesis. *Acc. Chem. Res.* **1981**, *14*, 16–21.
21. Hellman, A.; Honkala, K.; Remediakis, I.N.; et al. Ammonia Synthesis and Decomposition on a Ru-Based Catalyst Modeled by First-Principles. *Surf. Sci.* **2009**, *603*, 1731–1739. https://doi.org/10.1016/j.susc.2008.10.059.
22. Zhou, Y.; Wang, J.; Liang, L.; et al. Unraveling the Size-Dependent Effect of Ru-Based Catalysts on Ammonia Synthesis at Mild Conditions. *J. Catal.* **2021**, *404*, 501–511. https://doi.org/10.1016/j.jcat.2021.10.024.
23. Fang, H.; Liu, D.; Luo, Y.; et al. Challenges and Opportunities of Ru-Based Catalysts toward the Synthesis and Utilization of Ammonia. *ACS Catal.* **2022**, *12*, 3938–3954. https://doi.org/10.1021/acscatal.2c00090.
24. Zhang, T.; Zhang, X.; Chang, F. Synergistic Photothermal Acceleration of Ammonia Synthesis Using Defective TiO_2 Supported Ru Catalysts. *Ind. Eng. Chem. Res.* **2025**, *64*, 14879–14887. https://doi.org/10.1021/acs.iecr.5c02153.
25. Vieri, H.M.; Badakhsh, A.; Choi, S.H. Comparative Study of Ba, Cs, K, and Li as Promoters for Ru/$La_2Ce_2O_7$-Based Catalyst for Ammonia Synthesis. *Int. J. Energy Res.* **2023**, *2023*, 2072245. https://doi.org/10.1155/2023/2072245.
26. Altenburg, K. The Role of Potassium as a Promoter in Iron Catalysts for Ammonia Synthesis. *J. Catal.* **1980**, *66*, 326–334. https://doi.org/10.1016/0021-9517(80)90037-8.
27. Peng, X.; Luo, Y.; Zhang, T.; et al. Potassium Promoter Regulates Electronic Structure and Hydrogen Spillover of Ultrasmall Ru Nanoclusters Catalyst for Ammonia Synthesis. *Chem. Eng. Sci.* **2024**, *292*, 120021. https://doi.org/10.1016/j.ces.2024.120021.
28. Ye, T.N.; Park, S.W.; Lu, Y.; et al. Vacancy-Enabled N_2 Activation for Ammonia Synthesis on an Ni-Loaded Catalyst. *Nature* **2020**, *583*, 391–395. https://doi.org/10.1038/s41586-020-2464-9.
29. Zhuang, G.; Chen, Y.; Zhuang, Z.; et al. Oxygen Vacancies in Metal Oxides: Recent Progress towards Advanced Catalyst Design. *Sci. China Mater.* **2020**, *63*, 2089–2118. https://doi.org/10.1007/s40843-020-1305-6.
30. Huang, Y.; Yu, Y.; Yu, Y.; et al. Oxygen Vacancy Engineering in Photocatalysis. *Sol. RRL* 2020, *4*, 2000037. https://doi.org/10.1002/solr.202000037.
31. Humphreys, J.; Lan, R.; Chen, S.; et al. Improved Stability and Activity of Fe-Based Catalysts through Strong Metal Support Interactions Due to Extrinsic Oxygen Vacancies in $Ce_{0.8}Sm_{0.2}O_{2-\delta}$: Δfor the Efficient Synthesis of Ammonia. *J. Mater. Chem. A* **2020**, *8*, 16676–16689. https://doi.org/10.1039/d0ta05238h.
32. Nakaji, Y.; Kobayashi, D.; Nakagawa, Y.; et al. Mechanism of Formation of Highly Dispersed Metallic Ruthenium Particles on Ceria Support by Heating and Reduction. *J. Phys. Chem. C* **2019**, *123*, 20817–20828. https://doi.org/10.1021/acs.jpcc.9b00515.
33. Liu, Z.; Zhang, F.; Rui, N.; et al. Highly Active Ceria-Supported Ru Catalyst for the Dry Reforming of Methane: In Situ Identification of $Ru^{\delta+}$-Ce^{3+} Interactions for Enhanced Conversion. *ACS Catal.* **2019**, *9*, 3349–3359. https://doi.org/10.1021/acscatal.8b05162.
34. Li, C.; Shi, Y.; Zhang, Z.; et al. Improving the Ammonia Synthesis Activity of Ru/CeO_2 through Enhancement of the Metal–Support Interaction. *J. Energy Chem.* **2021**, *60*, 403–409. https://doi.org/10.1016/j.jechem.2021.01.031.
35. Lin, B.; Fang, B.; Wu, Y.; et al. Enhanced Ammonia Synthesis Activity of Ceria-Supported Ruthenium Catalysts Induced by CO Activation. *ACS Catal.* **2021**, *11*, 1331–1339. https://doi.org/10.1021/acscatal.0c05074.
36. Zhang, Z.Y.; Yao, J.L.; Pan, Y.Q.; et al. Strong Metal-Support Interaction Induced Excellent Performance for Photo-Thermal Catalysis Methane Dry Reforming over Ru-Cluster-Ceria Catalyst. *Nano Energy* **2025**, *133*, 110474. https://doi.org/10.1016/j.nanoen.2024.110474.
37. Kammert, J.; Moon, J.; Wu, Z. A Review of the Interactions between Ceria and H_2 and the Applications to Selective Hydrogenation of Alkynes. *Chin. J. Catal.* **2020**, *41*, 901–914. https://doi.org/10.1016/S1872-2067(19)63509-6.
38. Lin, B.; Liu, Y.; Heng, L.; et al. Morphology Effect of Ceria on the Catalytic Performances of Ru/CeO_2 Catalysts for Ammonia Synthesis. *Ind. Eng. Chem. Res.* **2018**, *57*, 9127–9135. https://doi.org/10.1021/acs.iecr.8b02126.
39. Liu, P.; Niu, R.; Li, W.; et al. Morphology Effect of Ceria on the Ammonia Synthesis Activity of Ru/CeO_2 Catalysts. *Catal. Lett.* **2019**, *149*, 1007–1016. https://doi.org/10.1007/s10562-019-02674-1.
40. Su, K.; Huang, D.; Fang, H.; et al. Boosting N_2 Conversion into NH_3 over Ru Catalysts via Modulating the Ru-Promoter Interface. *ACS Appl. Mater. Interfaces* **2023**, *15*, 56992–57002. https://doi.org/10.1021/acsami.3c12531.

41. Wang, Z.; Huang, Z.; Brosnahan, J.T.; et al. Ru/CeO_2 Catalyst with Optimized CeO_2 Support Morphology and Surface Facets for Propane Combustion. *Environ. Sci. Technol.* **2019**, *53*, 5349–5358. https://doi.org/10.1021/acs.est.9b01929.
42. Gao, Y.; Li, R.; Chen, S.; et al. Morphology-Dependent Interplay of Reduction Behaviors, Oxygen Vacancies and Hydroxyl Reactivity of CeO_2 Nanocrystals. *Phys. Chem. Chem. Phys.* **2015**, *17*, 31862–31871. https://doi.org/10.1039/c5cp04570c.
43. Liu, K.; Sun, Y.; Feng, J.; et al. Intensified Gas-Phase Hydrogenation of Acetone to Isopropanol Catalyzed at Metal-Oxide Interfacial Sites. *Chem. Eng. J.* **2023**, *454*, 140059. https://doi.org/10.1016/j.cej.2022.140059.
44. Sun, H.; Zhang, Y.; Wang, C.; et al. Integrated Carbon Capture and Utilization: Synergistic Catalysis between Highly Dispersed Ni Clusters and Ceria Oxygen Vacancies. *Chem. Eng. J.* **2022**, *437*, 135394. https://doi.org/10.1016/j.cej.2022.135394.
45. Morgan, D.J. Resolving Ruthenium: XPS Studies of Common Ruthenium Materials. *Surf. Interface Anal.* **2015**, *47*, 1072–1079. https://doi.org/10.1002/sia.5852.
46. Ma, Z.; Zhao, S.; Pei, X.; et al. New Insights into the Support Morphology-Dependent Ammonia Synthesis Activity of Ru/CeO_2 Catalysts. *Catal. Sci. Technol.* **2017**, *7*, 191–199. https://doi.org/10.1039/C6CY02089E.
47. Rakhmatullin, R.M.; Semashko, V.V.; Korableva, S.L.; et al. EPR Study of Ceria Nanoparticles Containing Different Concentration of Ce^{3+} Ions. *Mater. Chem. Phys.* **2018**, *219*, 251–257. https://doi.org/10.1016/j.matchemphys.2018.08.028.
48. Elmutasim, O.; Hussien, A.G.; Sharan, A.; et al. Evolution of Oxygen Vacancy Sites in Ceria-Based High-Entropy Oxides and Their Role in N_2 Activation. *ACS Appl. Mater. Interfaces*, **2024**, *16*, 23038–23053. https://doi.org/10.1021/acsami.3c16521.
49. Ho, C.; Yu, J.C.; Kwong, T.; et al. Morphology-Controllable Synthesis of Mesoporous CeO_2 Nano- and Microstructures. *Chem. Mater.* **2005**, *17*, 4514–4522. https://doi.org/10.1021/cm0507967.
50. Li, X.; Zhang, X.; Everitt, H.O.; et al. Light-Induced Thermal Gradients in Ruthenium Catalysts Significantly Enhance Ammonia Production. *Nano Lett.* **2019**, *19*, 1706–1711. https://doi.org/10.1021/acs.nanolett.8b04706.
51. Sousa, A.; Mateo, D.; Garzon-Tovar, L.; et al. Unlocking Low-Temperature Ammonia Decomposition via an Iron Metal–Organic Framework-Derived Catalyst Under Photo-Thermal Conditions. *Small* **2025**, *21*, 2411468. https://doi.org/10.1002/smll.202411468.
52. Bauer, C.; Abid, J.P.; Fermin, D.; et al. Ultrafast Chemical Interface Scattering as an Additional Decay Channel for Nascent Nonthermal Electrons in Small Metal Nanoparticles. *J. Chem. Phys.* **2004**, *120*, 9302–9315. https://doi.org/10.1063/1.1710856.
53. Liu, B.; Wu, H.; Parkin, I.P. Gaseous Photocatalytic Oxidation of Formic Acid over TiO_2: A Comparison between the Charge Carrier Transfer and Light-Assisted Mars–van Krevelen Pathways. *J. Phys. Chem. C* **2019**, *123*, 22261–22272. https://doi.org/10.1021/acs.jpcc.9b05357.
54. Xie, B.; Hu, D.; Kumar, P.; et al. Heterogeneous Catalysis via Light-Heat Dual Activation: A Path to the Breakthrough in C1 Chemistry. *Joule* **2024**, *8*, 312–333. https://doi.org/10.1016/j.joule.2023.12.013.
55. Collado, L.; Pizarro, A.H.; Barawi, M.; et al. Light-Driven Nitrogen Fixation Routes for Green Ammonia Production. *Chem. Soc. Rev.* **2024**, *53*, 11334–11389 https://doi.org/10.1039/d3cs01075a.
56. Mao, C.; Li, H.; Gu, H.; et al. Beyond the Thermal Equilibrium Limit of Ammonia Synthesis with Dual Temperature Zone Catalyst Powered by Solar Light. *Chem* **2019**, *5*, 2702–2717. https://doi.org/10.1016/j.chempr.2019.07.021.
57. Zheng, J.; Lu, L.; Lebedev, K.; et al. Fe on Molecular-Layer MoS_2 as Inorganic Fe-S_2-Mo Motifs for Light-Driven Nitrogen Fixation to Ammonia at Elevated Temperatures. *Chem Catal.* **2021**, *1*, 162–182. https://doi.org/10.1016/j.checat.2021.03.002.
58. Zhao, Y.; Miao, Y.; Zhou, C.; et al. Artificial Photocatalytic Nitrogen Fixation: Where Are We Now? Where Is Its Future? *Mol. Catal.* **2022**, *518*, 112107. https://doi.org/10.1016/j.mcat.2021.112107.
59. Choudhury, B.; Chetri, P.; Choudhury, A. Oxygen Defects and Formation of Ce^{3+} Affecting the Photocatalytic Performance of CeO_2 Nanoparticles. *RSC Adv.* **2014**, *4*, 4663–4671. https://doi.org/10.1039/c3ra44603d.
60. Peng, Y.; Albero, J.; Franconetti, A.; et al. Visible and NIR Light Assistance of the N_2 Reduction to NH_3 Catalyzed by Cs-Promoted Ru Nanoparticles Supported on Strontium Titanate. *ACS Catal.* **2022**, *12*, 4938–4946. https://doi.org/10.1021/acscatal.2c00509.
61. Rivera Rocabado, D.S.; Noguchi, T.G.; Hayashi, S.; et al. Adsorption States of N_2/H_2 Activated on Ru Nanoparticles Uncovered by Modulation-Excitation Infrared Spectroscopy and Density Functional Theory Calculations. *ACS Nano* **2021**, *15*, 20079–20086. https://doi.org/10.1021/acsnano.1c07825.
62. Lin, B.; Wu, Y.; Fang, B.; et al. Ru Surface Density Effect on Ammonia Synthesis Activity and Hydrogen Poisoning of Ceria-Supported Ru Catalysts. *Chin. J. Catal.* **2021**, *42*, 1712–1723. https://doi.org/10.1016/S1872-2067(20)63787-1.
63. Liu, P.; Huang, Z.; Yang, S.; et al. Support Amorphization Engineering Regulates Single-Atom Ru as an Electron Pump for Nitrogen Photofixation. *ACS Catal.* **2022**, *12*, 8139–8146. https://doi.org/10.1021/acscatal.2c01704.
64. Li, X.H.; Li, H.; Jiang, S.L.; et al. Constructing Mimic-Enzyme Catalyst: Polyoxometalates Regulating Carrier Dynamics of Metal-Organic Frameworks to Promote Photocatalytic Nitrogen Fixation. *ACS Catal.* **2023**, *13*, 7189–7198. https://doi.org/10.1021/acscatal.3c00944.
65. Feng, C.; Raziq, F.; Hu, M.; et al. Photoexcitation Altered Reaction Pathway Greatly Facilitate Ammonia Synthesis Over Isolated Ru Sites. *Adv. Energy Mater.* **2024**, *14*, 2303792. https://doi.org/10.1002/aenm.202303792.

66. Ooya, K.; Li, J.; Fukui, K.; et al. Ruthenium Catalysts Promoted by Lanthanide Oxyhydrides with High Hydride-Ion Mobility for Low-Temperature Ammonia Synthesis. *Adv. Energy Mater.* **2021**, *11*, 2003723. https://doi.org/10.1002/aenm.202003723.
67. Wang, Y.; Zhou, Y.; Huang, Y.; et al. Mechanistic Insights into Evolution of Schottky Junctions on Metal Nanoparticle-Loaded Mo-Doped TiO_2 for Enhanced Photothermal Ammonia Catalysis. *Chem. Eng. J.* **2025**, *517*, 164377.
68. Wang, Y.; Huang, L.; Zhang, T.C.; et al. Visible-Light-Induced Photocatalytic Oxidation of Gaseous Ammonia on Mo, c-Codoped TiO_2: Synthesis, Performance and Mechanism. *Chem. Eng. J.* **2024**, *482*, 148811. https://doi.org/10.1016/j.cej.2024.148811.
69. Peng, Y.; Melillo, A.; Shi, R.; et al. Light-Assistance in Nitrogen Fixation to Ammonia by Highly Dispersed Cs-Promoted Ru Clusters Supported on ZrO_2. *Appl. Catal. B Environ.* **2023**, *339*, 123143. https://doi.org/10.1016/j.apcatb.2023.123143.
70. Yang, Y.; Wang, P.; Zhang, X.; et al. Regulating the Scaling Relations in Ammonia Synthesis through a Light-Driven Bendable Seesaw Effect on Tailored Iron Catalyst. *Angew. Chem.* **2024**, *136*, e202408309.
71. Sousa, A.; Rendon Patino, A.; Garzon Tovar, L.; et al. Ammonia Decomposition via MOF-Derived Photothermal Catalysts. *ChemSusChem* **2025**, *18*, e202401896. https://doi.org/10.1002/cssc.202401896.
72. Bian, X.; Zhao, Y.; Waterhouse, G.I.N.; et al. Quantifying the Contribution of Hot Electrons in Photothermal Catalysis: A Case Study of Ammonia Synthesis over Carbon-supported Ru Catalyst. *Angew. Chem. Int. Ed.* **2023**, *62*, e202304452. https://doi.org/10.1002/anie.202304452.
73. Mao, C.; Wang, J.; Zou, Y.; et al. Photochemical Acceleration of Ammonia Production by Pt_1-Pt_n-TiN Reduction and N_2 Activation. *J. Am. Chem. Soc.* **2023**, *145*, 13134–13146. https://doi.org/10.1021/jacs.3c01947.
74. Li, X.K.; Ji, W.J.; Zhao, J.; et al. Ammonia Decomposition over Ru and Ni Catalysts Supported on Fumed SiO_2, MCM-41, and SBA-15. *J. Catal.* **2005**, *236*, 181–189. https://doi.org/10.1016/j.jcat.2005.09.030.
75. Yin, S.F.; Xu, B.Q.; Zhu, W.X.; et al. Carbon Nanotubes-Supported Ru Catalyst for the Generation of CO_x-Free Hydrogen from Ammonia. *Catal. Today* **2004**, *93–95*, 27–38. https://doi.org/10.1016/j.cattod.2004.05.011.
76. Duan, X.; Zhou, J.; Qian, G.; et al. Carbon Nanofiber-Supported Ru Catalysts for Hydrogen Evolution by Ammonia Decomposition. *Cuihua Xuebao/Chin. J. Catal.* **2010**, *31*, 979–986. https://doi.org/10.1016/s1872-2067(10)60097-6.
77. Yin, S.F.; Zhang, Q.H.; Xu, B.Q.; et al. Investigation on the Catalysis of CO_x-Free Hydrogen Generation from Ammonia. *J. Catal.* **2004**, *224*, 384–396. https://doi.org/10.1016/j.jcat.2004.03.008.
78. Yin, S.F.; Xu, B.Q.; Wang, S.J.; et al. Magnesia-Carbon Nanotubes (MgO-CNTs) Nanocomposite: Novel Support of Ru Catalyst for the Generation of CO_x-Free Hydrogen from Ammonia. *Catal. Lett.* **2004**, *96*, 113–116. https://doi.org/10.1023/B:CATL.0000030107.64702.74.
79. Rendon-Patiño, A.; Mateo, D.; Duran-Uribe, S.; et al. Ruthenium Nanoparticles within Carbon Spheres for Efficient Ammonia Decomposition. *ChemCatChem* **2024**, *93*, 27–38. https://doi.org/10.1002/cctc.202400878.